Saturation Gradients in Drainage of Porous Media: NMR Imaging Measurements

E. J. Fordham and L. D. Hall
Herchel Smith Laboratory for Medicinal Chemistry, Cambridge University School of Clinical Medicine, Cambridge, CB2 2PZ, U.K.

T. S. Ramakrishnan
Schlumberger-Doll Research, Old Quarry Road, Ridgefield, CT 06877

M. R. Sharpe and C. Hall
Schlumberger Cambridge Research, Cambridge, CB3 0HG, U.K.

A steady-state method recently proposed for measuring two-phase flow properties of a porous medium is supplemented by NMR imaging for measuring the saturation gradients which are allowed to persist in the specimen. The method relies on a strong capillary end effect which is assumed to be enforced by an outlet capillary pressure boundary condition, but direct verification of this has not hitherto been available. For constant flow rates, incremented stepwise, steady-state profiles of hydrocarbon saturation S_o are obtained which agree with predictions that they be monotonic, nonintersecting, and convex.

Using D_2O for the aqueous phase allows unambiguous detection of hydrocarbon by NMR, and imaging measurements of transverse relaxation time T_2 were included in the protocol. T_2 shows a dependence on S_o which is mild but not negligible for quantitative NMR imaging.

Introduction

A new steady-state technique for measuring some two-phase flow properties of a porous medium has recently been proposed (Ramakrishnan and Cappiello, 1991). The measurable properties of interest are nonwetting-phase relative permeability, capillary pressure and electrical resistivity. The method involves immiscible displacement of a wetting phase (typically water), by a nonwetting phase, a process known as *drainage*. Unlike traditional steady-state methods of relative permeability measurement, a phase saturation gradient is allowed to persist at all times through the sample; a zero capillary pressure boundary condition (equivalent to 100% water saturation) is enforced at the outlet by the presence of a pool of the wetting fluid. Such saturation gradients are the "capillary end effects" well known in work on two-phase flows in porous media (for example, Collins, 1961; Marle, 1981).

In the embodiment described by Ramakrishnan and Cappiello (1991), only integral measurements are made, and no provision exists for examining the shape of the steady-state saturation gradients. Because the method relies on the existence of the end-effect and its validity hinges on the assumption of a zero capillary pressure boundary condition, it is vital to verify this hypothesis. This is achieved for the first time in this work. The saturation profiles could in principle also yield useful information on other two-phase flow properties.

X-ray (Vinegar, 1986), microwave (Parsons, 1975) and gamma-ray (Graue et al., 1990) techniques have been used for imaging local saturation distributions in multiphase flows in porous media. We used a simple application of nuclear magnetic resonance (NMR) imaging for measuring the saturation distributions; the imaging method is, of course, applicable to other two-phase flow experiments in porous media. Various applications of NMR imaging to fluid and mass transport in porous media, including two-phase flows, have been proposed in recent years (Gummerson et al., 1979; Rothwell and Vinegar, 1985; Hall et al., 1986; Dereppe et al., 1990; Horsfield et al., 1990; Majors et al., 1990; Osment et al., 1990; Borgia et al., 1991a; Chen et al., 1992b). These almost exclusively have been

Correspondence concerning this should be addressed to E. J. Fordham, who is on leave from Schlumberger Cambridge Research Ltd.

applications of proton (^{1}H) NMR; such experiments are sensitive to hydrogen nuclei in water and hydrocarbons. A general advantage over alternative imaging methods is the variety of potential influences on image contrast (Callaghan, 1991), which allows for considerable flexibility in experimental design.

The price paid for this richness of image contrast factors is the need to eliminate or quantify the bias arising from other factors to concentrate on just one of them. Quantitative interpretation and the use of NMR imaging as a reliable *measurement* technique is, in consequence, less well-advanced, although the acquisition of mere contrast images can be straightforward.

In this work, we use isotopic substitution (D_2O in place of ordinary water) to render one phase "invisible" to ^{1}H NMR. Proton signal at echo times of a few milliseconds then arises unambiguously from the hydrocarbon component of the fluid saturation. We utilize the most basic module of Fourier NMR imaging: the spin echo under a single frequency-encoding ("read") field gradient. This provides profiles that are already integrated over the specimen cross section, and overall data acquisition times are short. A similar approach has been taken by Mandava et al. (1990) and Chen et al. (1992a). Although conceptually straightforward, using this method for quantitative phase saturation profiles requires: (i) calibration of signal levels against a known standard; (ii) attention to instrumental factors; and (iii) quantification of signal loss by transverse relaxation.

The latter is a fundamental bias inherent in any NMR spin-echo technique, imaging or otherwise, and can only be minimized by making the delay between initial excitation and the signal acquisition (the echo time T_E) short compared with the transverse relaxation time T_2. For the majority of porous media in typical NMR imaging systems, the shortest achievable T_E will not be sufficiently short for signal decay to be negligible. Quantification of this decay is thus fundamental to accurate estimates of liquid content in porous media. We also find that in our water-wet material, transverse relaxation in the non-wetting phase depends on local hydrocarbon saturation S_o, an observation difficult to make without an imaging experiment. Neglect of this variation cannot in general be correct, as recently pointed out by others (Chen et al., 1992b), although the assumption has been made in some previous work (Mandava et al., 1990).

With one empirical assumption in data fitting, we obtain hydrocarbon saturation profiles $S_o(y)$ in an experiment similar to that of Ramakrishnan and Cappiello (1991), for various steady states with constant hydrocarbon flow rates incremented stepwise. The shapes of these profiles constitute the principal fluid dynamical results of this work: they broadly agree with predictions that they be monotonic, nonintersecting, and convex; the expected capillary end effect, with vanishing exit hydrocarbon saturation, is clearly shown. We thus verify key assumptions of the method of Ramakrishnan and Cappiello (1991) for relative permeability measurement. Overall accuracy of the NMR method is assessed from comparison of the final profile with an independent gravimetric determination of final mean hydrocarbon saturation; these agree within 3% of pore volume.

Experimental: Materials and Apparatus

A schematic section of the rock core holder is shown in Figure 1a. A rock specimen, 38 mm diameter by 50 mm long, is mounted inside, sealed on its curved surface by a rubber sleeve, pressurized by a proton-free fluorocarbon oil. The cell is made of polyetheretherketone (PEEK), a proton-containing homogeneous engineering plastic, and is of significant mass compared to the fluids in the rock. The T_2 of the polymer's ^{1}H NMR signal, however, is very short (≈ 100 μs), so that in a spin-echo experiment with echo time $T_E \approx 2$ ms, any polymer signal will have decayed by a factor of about e^{-20}, entirely negligible for imaging purposes. Trial images of the completed cell without rock specimen or fluids yielded only noise.

At the inlet (lower) end, a spacer disc (PEEK) with a central hole of known volume V_{calib} provides an integral calibration reference. This is separated from the rock, physically and in the images, by another spacer disc, perforated with four fine holes for hydrocarbon flow.

At the outlet (upper) end, a plenum initially filled with D_2O is provided. This is the fundamental feature which maintains the zero capillary pressure outlet boundary condition. As hydrocarbon flows through the rock and reaches the outlet end, a fine stream ("mist") of hydrocarbon droplets rises and separates from the D_2O, subsequently flowing out through the fine tube. Initially some D_2O flows out also, but a steady level is rapidly reached (within 10 min), and subsequently only hydrocarbon exits; an adequate level of D_2O is maintained. Before each imaging exercise, excess hydrocarbon was removed from the surface of the D_2O pool and replaced with clean D_2O.

The rock used was Richemont limestone, a fine-grained carbonate used in France as a building stone (Honeyborne, 1982).

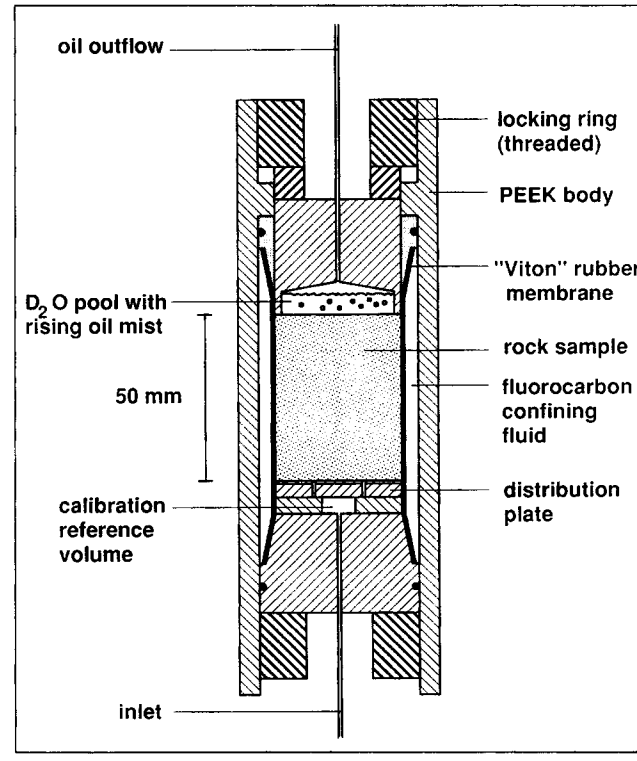

Figure 1a. Diametral section of the rock core holder.

Fluorocarbon confining fluid [Fluorinert FC-40, 3M Industrial Chemical Products Division] is pressurized at about 1 MPa by a HPLC pump; the cell passed hydraulic pressure tests at well above 3 MPa. Hydrocarbon outflow drains to atmospheric pressure. Hydrocarbon inflow is supplied at constant volumetric flow rates by a second HPLC pump.

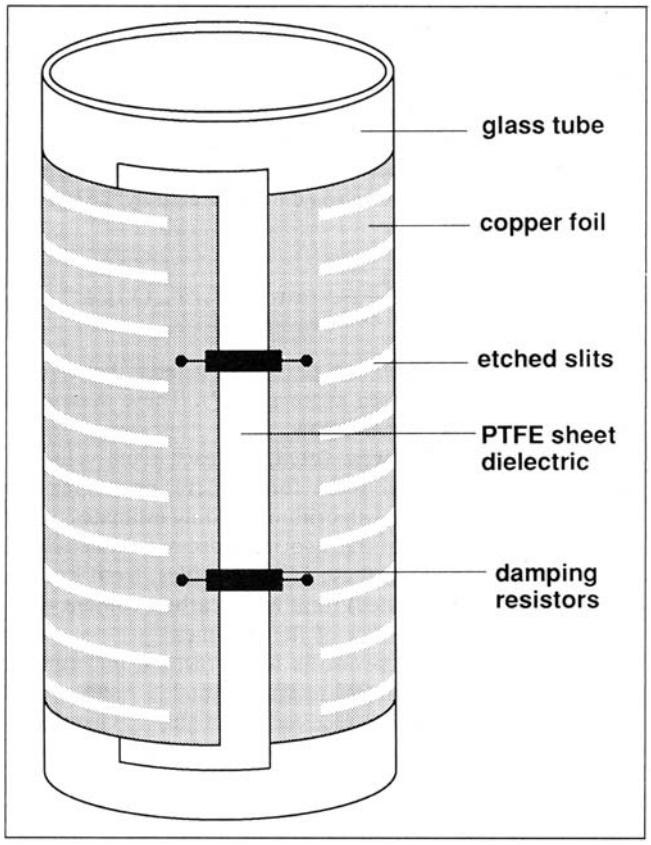

Figure 1b. Radio-frequency resonator (r.f. probe), inside which the cell in Figure 1a is mounted.

Axis orientation is vertical, transverse to the main magnet axis. Copper dimensions: 70 mm diameter, 100 mm long. Damping resistors are 10 kΩ, 2 W rating carbon types. The circumferential slots suppress eddy currents induced by gradient switching in imaging sequences and are etched in polymer-backed copper foil; the tube former is glass. Fully balanced capacitive coupling (by a half-wave loop balun, not shown) is used to provide a full "drop-through" access for the cell. R.f. (B_1) field maps were obtained by the method of Murphy-Boesch et al. (1987) as implemented by de Crespigny (1991); for diametral slices through the specimen in Figure 1a, the field was found to be uniform at least within one gray level in 34 (about ±3%).

Some petrophysical parameters are given in Table 1, and its NMR properties are discussed extensively below.

The sample was cut and then dried at 55°C for 24 hours in a *vacuum oven*; dry weight was measured, and grain volume and mean porosity $\bar{\phi}$ were determined in a helium pycnometer. The sample was evacuated again and then saturated with deaerated deionized water; the buoyancy method was used to check the porosity measurement and estimate any residual air saturation. NMR imaging profiles were obtained in the water-saturated state to plot local heterogeneities along the core axis. The specimen was then dried again in the vacuum oven, subsequently resaturated with 99.9% isotopic purity D_2O (Fluorochem Ltd.), and weighed suspended in hydrocarbon before mounting in the cell.

The hydrocarbon employed throughout this study was 99% pure *n*-dodecane (Aldrich Chemical Co. Ltd.). This was distilled to remove any trace contaminants with surface-active properties and pumped from an HPLC pump at constant flow rates, monitoring inlet pressure until this had stabilized. This

Table 1. Some Petrophysical Properties of Richemont Limestone*

Porosity (helium pycnometry)	0.286 (28.6 p.u.)
Permeability	
Nitrogen	2.7–14.5 μm^2
Water	1.9–10.2 μm^2
Typical pore throat sizes (mercury injection porosimetry)	
Entry diameter	10.3 μm
Median diameter (volume basis)	2.6 μm
Minimum diameter	0.72 μm

*Mercury injection porosimetry data ignore boundary effects in estimating early diameter. After the minimum pore size noted, negligible further intrusion occurred over more than two further decades of injection pressure to 414 MPa.

constant rate mode differs from the constant pressure control mode used by Ramakrishnan and Cappiello (1991), but is simpler to implement. Qualitatively similar results are expected, although quantitatively there may be errors introduced by capillary pressure hysteresis. At the lowest flow rates, several days were necessary before a stable pressure was reached, although this reduced to a few hours at the higher rates. In each identified steady state, NMR imaging was performed as detailed below to determine oil saturation profiles.

After the final images, the hydrocarbon flow was maintained until the D_2O pool had been removed (to avoid counterimbibition of heavy water) and then stopped. The buoyancy in dodecane was measured to determine (in conjunction with prior measurements) the final mean saturation in the specimen for comparison with the NMR data. The core was subsequently stored under dodecane; NMR relaxation measurements were then performed on the core in its final mixed saturation state.

The complete experiment was conducted over a period of nearly two weeks. Over such extended periods, there is a potential risk that even very slow leaks of fluorocarbon might accumulate within the core to significant levels. Fluorine-19 NMR was used to check for leakage. This nucleus has high instrinsic sensitivity and 100% natural abundance, and is present in high concentration in the confining fluid used, which gave a strong signal when tested in the bulk. No ^{19}F signal, however, was detectable from the rock specimen after two weeks in the cell.

NMR data were acquired using an Oxford Instruments 31 cm horizontal bore 2 T superconducting magnet and an Oxford Research Systems Biospec I console operating at 83.7 MHz for proton resonances. The (imaging) field gradient system was built on a 20 cm bore former; gradient strengths of up to 25 $mT \cdot m^{-1}$ were available within switching times of less than 200 μs. The experimental cell was mounted in a volume resonator ("probe") of the split-ring type (Hall et al., 1985), with some modifications shown in Figure 1b. These (cylindrical) resonators are mounted transverse to the main magnet axis; this was a requirement in this experiment where buoyancy was used to separate the phases in the outflow system.

The pulse sequence of the NMR protocol used is illustrated, approximately to scale, in Figure 2. This one-dimensional profiling method is the basis of all spin-echo Fourier imaging. An outline of imaging theory is given for reference in the Appendix; detailed discussions of the physics of NMR may be found in the standard texts (for example, Abragam, 1961; Slichter,

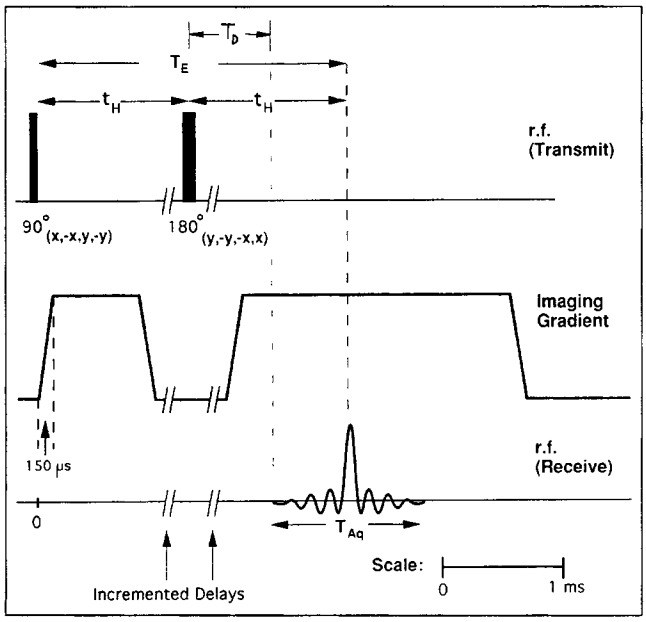

Figure 2. Timing (approximately to scale) of the one-dimensional imaging (profile-generating) pulse sequence.

Repolarization delays (not shown) of 8 s are included between all repetitions. Subscripts to the pulse length indicate the phase-cycling scheme used to eliminate d.c. offsets and balance channel gains. Two cycle repetitions providing a total of 8 signal accummulations were used. The entire sequence is repeated through fifteen 500 μs increments in T_E (minimum 2.616 ms) with a total data acquisition time of about 17 minutes. Spectral width $W_A = 100$ kHz; acquisition window $T_{Aq} = 1.28$ ms for 128 complex points. Gradient strength $G_y = 23.63$ mT·m^{-1} (10.06 kHz·cm^{-1}). Pixel width $2\pi\Delta\nu_p/\gamma G_y = 0.783$ mm. 90° pulse width typically 45 μs.

1990) and of imaging in the texts of Callaghan (1991) or Mansfield and Morris (1982).

To obtain additional data on signal decay by transverse relaxation, the acquisition was repeated through 15 increments of T_E (Figure 2), yielding a set of magnetization profiles $M(y; T_E^{(i)})$ $(i = 0, \ldots, 15)$, where y is the vertical coordinate. Data acquisition time is less than 12 ms for each scan; the dominant delay in the whole arrangement is the longitudinal magnetization recovery time T_R of 8 seconds allowed between all scans. A fourfold cycling of r.f. phase (Figure 2) is also used to correct for d.c. offsets and quadrature imbalance; this is repeated twice for further signal averaging. Total instrument time required for each imaging exercise in the intermediate steady states was only 17 minutes.

Data Analysis: Evaluation of Saturation Profiles

The measured data $M(y; T_E^{(i)})$ are related to the section average proton (^{1}H) density:

$$\bar{\varrho}_s(y) = \int_{\text{section}} \varrho(x)\,dx\,dz \tag{1}$$

(where $\varrho(x)$ is the local proton density) by:

$$\frac{1}{s} M(y; T_E) = \bar{\varrho}_s(y)\, g(T_E; y). \tag{2}$$

In Eq. 2, s is a (constant) scale factor and $g(T_E; y)$ is a signal decay model satisfying $g(T_E; y) \le 1$ with equality where $T_E = 0$. For the simple exponential model $g(T_E; y) = \exp[-T_E/T_2(y)]$, Eq. 2 is derived in the Appendix. However, the simple exponential model lacks a theoretical basis and is not necessarily quantitative. Although still entirely empirical, a more flexible description of actual relaxation data is offered by the stretched exponential form:

$$g(T_E; y) = \frac{M(y; T_E)}{M(y; 0)} = \exp\{-[T_E/T_{2\alpha}(y)]^{\alpha}\} \tag{3}$$

where α may be either <1 or >1 (the latter being better described as "compressed exponential"). These descriptions will be considered further below.

The data $M(y; T_E^{(i)})$ were fitted, for each fixed value of y in turn, to this model form for $g(T_E; y)$ by a maximum likelihood (least squares) algorithm, yielding estimates of both $M_0(y) \equiv M(y; 0)$ and of the associated decay parameters such as $T_{2\alpha}(y)$. We interpret these $M_0(y)$ profiles, from Eq. 2, as $s\bar{\varrho}_s(y)$, that is, the (scaled) total hydrocarbon content within a particular transverse slice of the specimen.

The scale factor s depends on many factors, including the static field B_0, temperature, resonator quality factor Q, and the gains of preamplifier, receiver and digitizer. Given stable temperature and hardware, it, however, may be taken as a constant in a particular experiment. The entire imaging experiment was directly calibrated for hydrocarbon volume by using the integral calibration volume in the cell. Calibration is thus strictly contemporary with data acquisition; drifts in gains, fields and temperature, and variations in probe Q (and hence, sensitivity) caused by variations in probe "loading" from image to image are all irrelevant.

The final conversion to a local saturation fraction is made by normalizing the hydrocarbon profiles against a local porosity profile. The profile acquired with the specimen in its water-saturated state $M_0^{(w)}(y)$ is interpreted as a profile of section average porosity $\phi(y)$. In this case, no absolute calibration was necessary, since the mean porosity $\bar{\phi}$ was available from helium pycnometry and buoyancy data obtained during core preparation; the magnetization profile was simply rescaled:

$$\phi(y) = \frac{\bar{\phi} M_0^{(w)}(y) L_{\text{rock}}}{\int_{\text{rock}} M_0^{(w)}(y')\,dy'} \tag{4}$$

Magnetization profiles $M_0^{(o)}(y)$ obtained during the subsequent drainage (dodecane displacing D_2O) are profiles of hydrocarbon signal only. In these cases, the calibration volume was available. Together with the profile $M_0^{(w)}(y)$, they were used to construct profiles of local hydrocarbon phase saturation fraction $S_o(y)$; the segment of $M_0^{(o)}(y)$ corresponding to the rock is scaled according to the segment corresponding to the calibration reference and its known volume, and again according to the porosity profile derived from $M_0^{(w)}(y)$ and Eq. 4:

$$S_o(y) = \frac{M_0^{(o)}(y) V_{\text{calib}} \int_{\text{rock}} M_0^{(w)}(y')\,dy'}{M_0^{(w)}(y) \bar{\phi} V_{\text{rock}} \int_{\text{calib}} M_0^{(o)}(y')\,dy'}. \tag{5}$$

For both $M_0^{(w)}(y)$ and $M_0^{(o)}(y)$, the data fitting also yields profiles of the associated transverse relaxation times $T_{2\alpha}^{(w)}(y)$ and $T_{2\alpha}^{(o)}(y)$. These are discussed below.

NMR Relaxation of Liquids in Richemont Limestone

Longitudinal relaxation

The longitudinal relaxation time T_1 does not appear in Eq. 2, which assumes that each scan begins with the nuclear spin system in its fully polarized (thermal equilibrium) state. Although for sufficiently long T_R the exact value of T_1 is irrelevant, an approximate value is required to choose an adequate T_R. The physics of T_1 relaxation is also of interest in its own right, because of connections with wettability and pore size.

For a wetting phase, surface processes usually dominate the overall relaxation rate (Banavar and Schwartz, 1989), and in pores of "size" a (volume to surface ratio) this is itself dominated by a single mode of rate $1/T_{1S}=\rho_1/a$ (where ρ_1 is a surface relaxivity), provided that $\rho_1 a/D \ll 1$, D being the molecular diffusivity (Brownstein and Tarr, 1979). This limit nearly always holds for water-saturated rocks (Latour et al., 1992). A distribution of pore sizes implies a distribution of relaxation times $1/T_{1S}$; magnetization from many pores then shows multiexponential behavior (unless the porous medium contains only a single pore size, an improbable situation for natural rocks). For routine purposes (Kenyon et al., 1988), this may be described by the stretched exponential. Parameter values for water-saturated Richemont limestone are given in Table 2.

In more detailed analysis, a full spectrum of relaxation times may be assumed, and a suitably regularized data analysis then provides an indication of the underlying pore-size distribution (Gallegos and Smith, 1988; Kenyon et al., 1989; Davies and Packer, 1990; Latour et al., 1992). An example (water-saturated Richemont limestone) is shown in Figure 3. This may be interpreted as a distribution of pore volume to surface ratios

Table 2. Longitudinal (T_1) Relaxation Times Determined at 83.7 MHz for ^{1}H Resonance of Fluids in the Bulk and in the Richemont Limestone Matrix*

Fluid & State	Stretched exponential		Biexponential	
	$T_{1\alpha}$	α	T_1	Magnetization Fraction
Water saturation in rock	146 ms	0.79	—	—
Bulk water (deionized, deaerated)	2.55 s	1.00	—	—
Dodecane in rock, mixed saturation (D_2O/dodecane)	1.23 s	0.98	—	—
Bulk dodecane	1.18 s	1.00	1.30 s	5.88/26
	—	—	1.15 s	20.1/26

*The inversion-recovery method was used. Biexponential T_1 values for bulk dodecane agree well with chemical shift resolved null point estimates of T_1 for the methyl and methylene resonances. Magnetization partitions are close to the expected 6:20 ratio. These T_1 data, however, are sufficiently close to that at 83.7 MHz, and at 22°C the relaxation can be adequately represented by a single exponential model. Data acquired in an air-conditioned laboratory (approximately 22°C) but not in temperature-controlled probes.

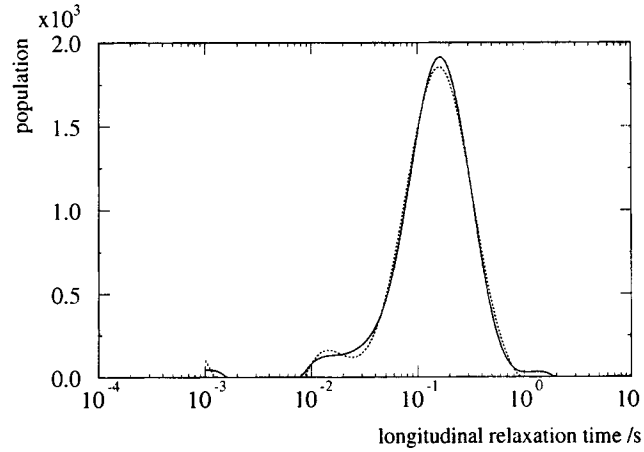

Figure 3. Regularized distribution of T_1 for Richemont limestone (water-saturated) with optimum regularization determined by the method of Butler et al. (1981) as implemented by Sezginer (Kenyon et al., 1989; Latour et al., 1992).

Inversion recovery data with 64 recovery times logarithmically spaced between 850 μs and 2.5 s were used. The specimen was the same size and came from the same block as that used in the drainage experiment. Continuous and dotted curves indicate repeatability.

a, with the unknown parameter ρ_1 as a scale factor. Independent indication of pore-size distribution can be obtained by mercury intrusion porosimetry. This technique is sensitive to throat size, rather than pore body size, but the two may be expected to be correlated. The width of the size distribution obtained from mercury porosimetry is approximately a factor of 15 (Table 1), similar to the width in Figure 3.

With two immiscible liquid phases present, a wholly or preferentially wetting phase may prevent nonwetting-phase molecules diffusing to the surface. The bulk relaxation rate may then dominate in the nonwetting phase, although relaxation is not necessarily monoexponential, if ^{1}H nuclei in the liquid molecules are chemically inequivalent. This is the case for the methyl and methylene group protons in hydrocarbons, but the difference for n-dodecane turned out to be small (see Table 2 legend). In Richemont limestone, there is nearly an order of magnitude difference in $T_{1\alpha}$ for the two saturation states (Table 2). When water-saturated, a stretched exponential model is required to fit the data whereas for the dodecane/D_2O saturation a single exponential model was adequate. The dodecane $T_{1\alpha}$ value found was then close to that for bulk dodecane. These data are indicative of a pore surface material, which is water-wet, at least to the extent of a thin film of "pellicular" water (Buckley et al., 1989). Similar observations have been made (for other media) by Borgia et al. (1991b).

Transverse relaxation

Both bulk and surface relaxation mechanisms also apply to transverse (T_2) relaxation in porous media, but a third mechanism must also be considered, spin dephasing by molecular diffusion within the internal field gradients g_0 which arise from the mismatch of magnetic susceptibility between grain material and the pore fluid. In many porous media, this is the dominant

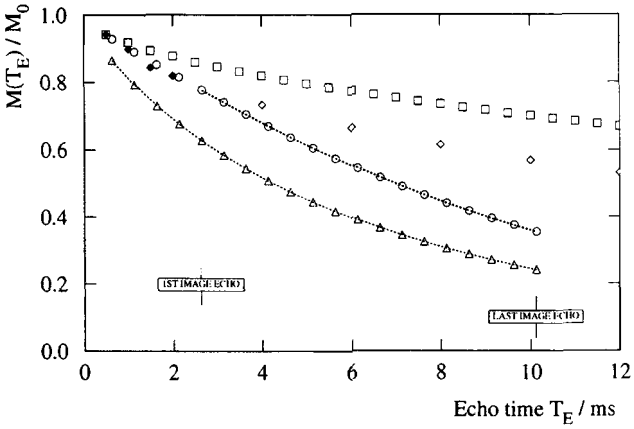

Figure 4. Simple Hahn echo ($90_x - t_H - 180_y - t_H$ – Acquire) amplitudes as a function of $T_E = 2t_H$ for the ^1H signal from the main test specimen.

Four signal averages were used. Data normalized against contemporary FID amplitudes obtained with back extrapolation through the instrumental dead time of 100 μs. Parameter values from data fitting are in Table 3. The graph is restricted to T_E values used in the imaging experiments (shown). $\triangle$ (water only saturation) and o (mixed-phase saturation) obtained after the main drainage experiment was completed; — — — —, fitted curves over indicated data range. Some CPMG echo amplitudes are shown (mixed-phase saturation state only): ♦, first echo amplitudes in CPMG echo trains (t_{CP} = 250, 500, 750, 1,000 μs, respectively); □, full CPMG envelope at t_{CP} = 250 μs; ◇, full CPMG envelope at t_{CP} = 1 ms.

mechanism of transverse relaxation at the field strengths typical of imaging systems (Kleinberg and Horsfield, 1990).

This physics of transverse relaxation is subtle. No comprehensive theory exists, so an empirical model is necessary for interpretation of the data. The model chosen was suggested from bulk specimen relaxation results given below. The comparability of bulk and imaging relaxation data may be questioned for two reasons: (i) the imaging gradient G_y may add significantly to g_0; (ii) dispersive molecular motions may be increased by fluid flow and hydrodynamic dispersion in the drainage experiment. Both would increase the diffusional attenuation which is the dominant factor in transverse relaxation. However, estimates of g_0 were two orders of magnitude greater than G_y, and echo amplitudes with and without G_y were shown to be negligibly different; similarly, advective flow distances $\bar{v}T_E$ were also small compared with molecular diffusion distances $(DT_E)^{1/2}$.

Results for our main test specimen, in the reference water-saturated state and in the final mixed-phase saturation state (D_2O and dodecane), are shown in Figure 4 and Table 3. Figure 4 shows peak amplitudes of the single ("Hahn," after Hahn, 1950) spin echo as a function of T_E for the two states. The T_E range displayed is restricted to that used in the imaging experiments, although data were obtained at longer T_E. In the water-saturated state, the Hahn echo envelope is fit adequately by a stretched exponential (Eq. 3) with a stretching exponent α of 0.83. In the mixed-phase state, a value of 1.12 is required for α. We conjecture that the difference in shape is because of (i) the hydrocarbon distribution avoiding small or dead-end pores, and thus being quite different to the single-phase water distribution, and (ii) the absence of surface relaxation, as demonstrated by the T_1 data. The effect of data span on fitted parameter estimates is illustrated in Table 3. Early echo amplitudes of some multiple-echo trains (for the mixed saturation sample only) are also shown. The multiple echo ("CPMG") sequence used was that of Carr and Purcell (1954) with the modification of Meiboom and Gill (1958). The amplitudes of the first echoes of the CPMG trains agree (as they should) with the Hahn echo envelope.

It is apparent from Table 3 that assigning a single T_2 value "of the specimen" is meaningless. Values depend on the protocol used in the CPMG method on the spacing t_{CP} and as shown by Kleinberg and Horsfield (1990) on the field strength B_0 (with which the internal background gradients g_0 scale). Describing the decay may require either stretched or compressed exponential forms, and values derived from fitting to these entirely empirical models may depend somewhat on the data span taken. Finally, as will be seen from the imaging results, the $T_{2\alpha}^{(o)}$ values depend on local hydrocarbon phase saturation to a degree that cannot be neglected.

Actual envelopes of T_2 decay were therefore used in our imaging experiment to obtain the estimates of local $M_0(y)$ by extrapolation to $T_E = 0$ pixel by pixel (Eqs. 2 and 3). This strategy has also been adopted by Chen et al. (1992b). We used the Hahn echo envelope, but either type in principle could have been used. For short spans ($T_E \leq 10$ ms) of bulk specimen data (Table 3, Figure 4), the stretched/compressed exponential

Table 3. Transverse (T_2) Relaxation Parameters for the Data of Figure 4*

Specimen State	T_E Range/ms	No. of Echoes	Envelope Type	t_{CP}/μs	$T_{2\alpha}$/ms	α	Relative M_0 (Fitted)
Water saturated	0.6–32	64	Hahn	—	6.55	0.82	1.02
	0.6–10	20		—	6.66	0.83	1.01
	2.6–10	16		—	6.62	0.83 (fixed)	1.01
Mixed-phase saturation (D_2O/dodecane)	0.6–32	64		—	10.0	1.06	1.01
	0.6–10	20		—	10.1	1.12	1.00
	2.6–10	16		—	10.1	1.12 (fixed)	1.00
	0.5–12	24	CPMG	250	49.5	0.67	1.01
	0.5–256	512		250	46.2	0.60	1.06
	1.0–512	512		500	31.1	0.56	1.10
	1.5–768	512		750	19.8	0.53	1.14
	2.0–12.0	6		1,000	24.4	0.65	1.02
	2.0–512	256		1,000	20.1	0.53	1.15

*M_0 values are normalized against contemporary FID amplitudes (back-extrapolated through the instrumental dead time of 100 μs) with allowance made for short-lived probe background signal at the level of 2.5% and 1.25% of observed M_0, respectively, for the mixed phase and water saturation states.

model (Eq. 3) appears to model the decay envelope well. Because the imaging data are unavailable for $T_E < 2.6$ ms, we chose to model the *shape* of the decay by fixing the exponent α at its bulk specimen value. Both M_0 and the scale parameter $T_{2\alpha}(y)$, however, were left free. Table 3 shows that, for bulk data, fixing α at a previously determined value and eliminating the echoes for $T_E < 2.6$ ms result in negligible changes in values of the fitted parameters M_0 and $T_{2\alpha}$.

Fixing the value of α for analyzing the imaging data is an empirical assumption about the shape of the decay envelopes for individual pixels, but some such assumption is implicit in any model extrapolation, pending a better understanding of the physics of the relaxation law. The value of α used, however, was found from bulk data which covered the range $T_E < 2.6$ ms. Also, while avoiding the potential distortions arising from a single exponential model [by modeling the shape of the decay near $T_E = 0$], fixing α results in a one-parameter description of the timescale $T_{2\alpha}$ of the decay [at least for the early stages $M(T_E)/M_0 > 1/e$]. This makes possible a compact assessment of the influence of oil saturation S_o on $T_{2\alpha}$ (discussed below), which is not available with multiparameter descriptions.

Chen et al. (1992a,b) report unsatisfactory results in determinations of mean porosity when using the stretched exponential form for extrapolation and prefer a biexponential model. Table 3 confirms that large errors in M_0 estimates are possible when using the stretched exponential over a large span of T_E; the model does not fit well enough over large ranges. Also, for $\alpha < 1$, the model has infinite slope at the origin, which can lead to unstable extrapolation. The biexponential model, having three adjustable parameters describing the shape of the decay in addition to the M_0 estimate, naturally provides a closer fit. However, because our primary measurement objective was M_0, our imaging data were analyzed only for the early range of T_E (2.6–10 ms), for which oil signal levels are still above M_0/e (Figure 4); data in the "tail" of the decay envelope were not used. Also, when $\alpha > 1$ (as for our hydrocarbon data), the model has *zero* slope at the origin; extrapolations then suffer less instability than for $\alpha < 1$.

The adequacy of our model, over the data range used, can be quantified by computing profiles of the mean square misfit $\chi^2(y) = (1/N)\,\Sigma_i^N [M(y; T_E^{(i)})/M_0(y) - g(T_E^{(i)}; y)]^2$ for the image profiles discussed below. For the water profile $M_0^{(w)}(y)$, we found $0.001 < \chi(y) < 0.003$ except for a few noisy pixels. For the oil profiles $M_0^{(o)}$, the range $0.002 < \chi(y) < 0.015$ was representative except for pixels in the last cm where M_0 drops toward zero and signal-to-noise ratio is poor.

Results of the Capillary Drainage Experiment

For our specimen in its initially fully water-saturated state, the fitted magnetization profile $M_0^{(w)}(y)$ is shown in Figure 5a with the corresponding profile of $T_{2\alpha}^{(w)}(y)$ shown in Figure 5b. Note that these profiles show a 6-cm-long core; this was cut down to 5 cm before use in the drainage experiment.

Magnetization profiles $M_0^{(o)}(y)$ obtained during the drainage experiment are shown in Figure 6, derived by the data fitting described above and rescaled to give a constant integral over the calibration volume of the core holder. Obvious features of the overall profiles are annotated. The associated steady inlet pressures are not discussed further here, but are included as a function of the flow rate in Figure 7. Finally,

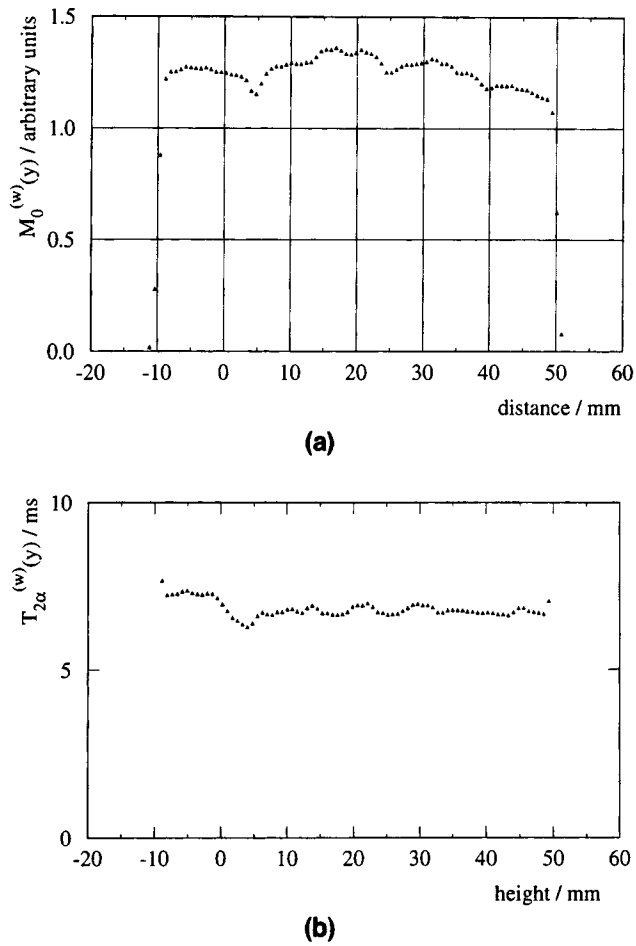

Figure 5. (a) Profile of estimated total magnetization $M_0^{(w)}(y)$ (arbitrary units) for the main test sample in the reference water saturated state; (b) corresponding profile of $T_{2\alpha}^{(w)}$.

Note that this profile is for a 60 mm long specimen; this was reduced to 50 mm for the main drainage experiment by removal of the (−10 mm, 0 mm) region. Data fitting of raw profiles at various T_E performed by the method described in the text to the model suggested by Figure 4. Fixed $\alpha = 0.83$ (Table 3).

local oil saturation profiles $S_o(y)$ are shown in Figure 8a. These were derived according to Eq. 10, from the data of Figures 5a and 6. The associated profiles of $T_{2\alpha}^{(o)}(y)$ are shown in Figure 8b.

A standard spin-warp image (Edelstein et al., 1980) of the specimen in the final state is shown in Figure 9. Such images are powerful aids to the interpretation of the simpler profile data, even without full quantification. Various heterogeneities can be identified which correlate with features in the profiles. One can check that the calibration volume is full, without trapped air bubbles. A drop of bulk dodecane was trapped for the duration of the experiment between a small chip in the specimen edge and the edge of the upper end plug (Figure 1a); this can be seen at the upper right in Figure 9. It was also evident in a similar image (not shown) taken in the initial state, when the specimen (D_2O saturated) was invisible. This nuisance feature obtrudes somewhat in the profile data at all stages and obscures the exact rock outlet position in the profiles, but is easily identified in the full image.

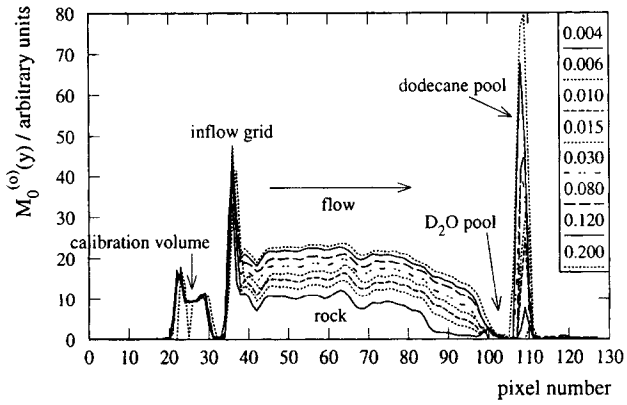

Figure 6. Magnetization profiles obtained in the main capillary drainage experiment; $M_0^{(o)}(y)$ data fitted from the full data set over various T_E and rescaled such that the integral over the calibration volume is 100 units.

Major features identified. Data acquired in steady flow pressure conditions at incremented constant flow rates; numbers in legend are volumetric flows in $cm^3 \cdot min^{-1}$. Single zero point in calibration volume at 0.015 $cm^3 \cdot min^{-1}$ is artifact arising from spatial misregistration of one profile.

General features of the saturation profiles

The oil saturation profiles of Figure 8a show the qualitative behavior predicted by the theory of Ramakrishnan and Cappiello (1991). According to their theory, for a homogeneous and uniform medium at steady state the oil superficial velocity q through the medium may be expressed as:

$$q = -\frac{kk_{ro}(p_c)}{\mu_o}\frac{dp_c}{dy} \tag{6}$$

where k is the permeability of the medium, μ_o is the hydrocarbon viscosity, and p_c is the capillary pressure. In Eq. 6, because the D_2O is stationary, q is also the total superficial velocity and the oil pressure gradient is given by the capillary pressure gradient. Also, note that the relative permeability to oil k_{ro} has been expressed as a function of p_c. Since p_c is a

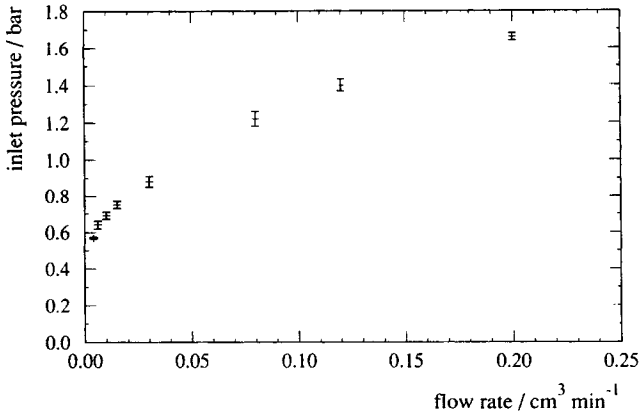

Figure 7. Steady-state inlet pressures for the incremented constant flow rates.

The principal contributors to the error bars are fluctuations arising from a rock stress effect when the confining pressure control passed through its hysteresis dead band.

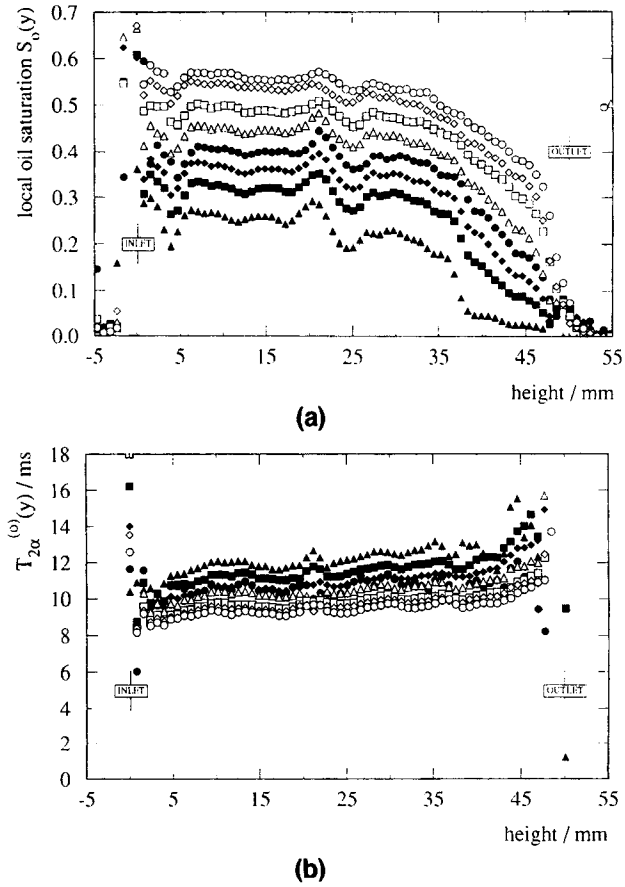

Figure 8. (a) Hydrocarbon saturation profiles $S_o(y)$ derived from the data of Figures 6 and 5a; (b) corresponding profiles of $T_{2\alpha}^{(o)}$.

Magnetization profiles of Figure 6 scaled for dodecane volume equivalent according to the known calibration volume and locally by the porosity profile of Figure 5a. This scaling is only meaningful within the rock although a few data points outside the rock specimen region are also shown. Rock inlet and outlet stations annotated. The small peak shown near the rock outflow in the early saturation profiles is from a drop of bulk dodecane trapped between the D_2O plenum plug in Figure 1a and in a small chip in the rock. Part of this drop can be seen in the full image of Figure 9. Fixed $\alpha = 1.12$ (Table 3). Data in the chip region noted in (a) rises rapidly off the displayed scale, consistent with a significant fraction of bulk liquid signal in those pixels. Volumetric flows in $cm^3 \cdot min^{-1}$: ▲ 0.004; ■ 0.006; ◆ 0.010; ● 0.015; △ 0.030; □ 0.080; ◇ 0.120; ○ 0.200.

monotonically decreasing function of S_w ($dp_c/dS_w < 0$), relative permeability may be alternatively expressed as a function of S_w. Various general properties of the saturation profiles may be deduced as follows.

First note from Eq. 6 that for q and kk_{ro}/μ_o positive, $dp_c/dy < 0$. Since $dp_c/dS_w < 0$, we see that $dS_w/dy = (dp_c/dy) \cdot (dS_w/dp_c) > 0$, and so $S_w(y)$ is monotonically increasing. Equivalently, the oil saturation profile $S_o(y)$ decreases monotonically.

Now integrate Eq. 6 from the outlet ($y = L_{rock}$) to an arbitrary position y to obtain:

$$q(L_{rock} - y) = \int_0^{p_c(y)} \frac{kk_{ro}(p_c)}{\mu_o}\, dp_c. \tag{7}$$

The integrand is always positive, so clearly $p_c(y)$ increases

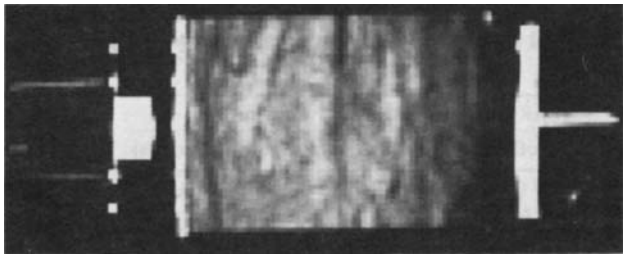

Figure 9. Standard spin-warp image of the experimental cell in the final flow state (corresponding to the final profile in Figures 6 and 8a).

128^2 pixels, no display interpolation applied. Read gradient as for profile data. Slice thickness 5 mm selected by a 3 ms band selective 180° pulse (Roberts, 1992). Echo time $T_E = 5.53$ ms. Inlet tubes, calibration volume, distribution grid and dodecane layer floating on top of the D_2O pool (dark) show bright; heterogeneities in the rock corresponding to those seen in the profiles can also be identified. Part of the trapped dodecane drop seen at 48–50 mm in Figures 6 and 8a is visible at the upper right of the rock. Image display with "read" gradient direction horizontal is conventional for NMR imaging. Physical orientation as in Figure 1a.

with flow q, at any position y. Equivalently, since $dp_c/dS_w < 0$, S_w decreases with flow q at any position y. Hence, saturation profiles $S_w(y)$ or $S_o(y)$ for different flow rates q or different inlet pressures cannot intersect.

For an infinite medium, the entry capillary pressure is determined by the critical percolation probability of the underlying pore network (Ramakrishnan and Wasan, 1986). For reasonable pore-size distributions, the qualitative aspects of the capillary pressure curve are determined by percolation-like processes. Typically then, large saturation changes occur close to the entry capillary pressure. We thus expect $p_c(S_w)$ not only to be monotonically decreasing, but also concave, that is, $d^2p_c/dS_w^2 > 0$. Independent capillary pressure measurements (to be reported elsewhere) in a sample from the same block show this to be true except for small finite-size effects near the entry capillary pressure. For such a capillary pressure curve, we may also deduce that the oil saturation profile is convex.

Differentiating Eq. 6 with respect to y, we obtain:

$$k_{ro}(p_c)\frac{d^2p_c}{dy^2}+\frac{dk_{ro}}{dp_c}\left(\frac{dp_c}{dy}\right)^2=0. \tag{8}$$

Now, it is a feature of relative permeability curves that $dk_{ro}/dp_c > 0$. Thus, from Eq. 8, $d^2p_c/dy^2 < 0$. Given that p_c is an explicit function of S_w we also have:

$$\frac{d^2p_c}{dy^2}=\frac{d^2p_c}{dS_w^2}\left(\frac{dS_w}{dy}\right)^2+\frac{dp_c}{dS_w}\frac{d^2S_w}{dy^2}. \tag{9}$$

In Eq. 9, we have from previous statements that $d^2p_c/dy^2 < 0$, $d^2p_c/dS_w^2 > 0$ and $dp_c/dS_w < 0$. Hence, $d^2S_w/dy^2 > 0$, or equivalently $d^2S_o/dy^2 < 0$, which shows the convexity of $S_o(y)$.

The *general* behavior of the data supports the qualitative results presented above. Except for fluctuations attributable to local porosity and permeability variations, the oil saturation profiles at various flow rates decrease monotonically and are strictly nonintersecting. Apart from the two lowest flow rates, where it is possible that true steady states had not in fact been reached, the profiles are generally convex. The presence of end-effect is clearly seen at the exit where the rock remains completely water-saturated. This, therefore, implies an infinite oil pressure gradient at the exit. These results clearly support the assumptions of Ramakrishnan and Cappiello (1991), directly verified here for the first time. They also have strong implications for much of core flooding research, where it is a common practice to flow several pore volumes of oil to attempt to reach residual water saturation. We see that due to end-effects it is the flooding *rate*, rather than cumulative throughput, which is important in reaching residual water; at any one flow rate, a steady state is reached after which further oil flow has no effect on saturation.

Saturation-dependence of T_2

The associated $T_{2\alpha}^{(o)}(y)$ profiles shown in Figure 8b show a distinct slope in all cases, apparently associated with the profile $S_o(y)$, and a systematic reduction as the mean hydrocarbon saturation level rises. These data are strongly suggestive of a dependence of $T_{2\alpha}^{(o)}$ on local hydrocarbon saturation S_o. The data are also plotted in a $(T_{2\alpha}^{(o)}, S_o)$ scatter plot in Figure 10a. A satisfactory collapse of the data about a common trend is seen; a small improvement in the collapse is obtained when the ratio of local $T_{2\alpha}^{(o)}$ in the mixed saturation state to the corresponding $T_{2\alpha}^{(w)}$ in the water saturated state is similarly plotted (Figure 10b).

This dependence is of considerable practical importance for work of this kind; although the variation is mild, it does amount to a factor of 2 over the full saturation range 0–100%. At the T_E/T_2 ratios typical of practical systems, this variation cannot be neglected and justifies the approach taken in characterizing the decay locally within the images. Assumptions of a constant T_2 would be incorrect. Physically, the dependence is understandable on the basis of hydrocarbon distribution among pores of various sizes. For low hydrocarbon saturations, it is likely to be distributed among the larger pores. Larger pores will tend to have weaker internal gradients. The dominant diffusion effects discussed above (Transverse Relaxation) may thus be expected to be weaker at low S_o. The general trend of Figure 10 is consistent with this qualitative picture.

Accuracy

The sensitivity in the profile experiment is subject to a combination of systematic errors arising from inhomogeneity in B_0 and G_y, eddy current fields, inhomogeneity in B_1 (particularly in reception), and overall frequency response of probe, analogue filters and spectrometer. Each factor was addressed and minimized experimentally, but quantification of individual contributions to the error at the level of a few percent is difficult. The overall result, however, was determined experimentally with a uniform cylindrical phantom filled with doped water. There was a small systematic taper at the top (corresponding to the D_2O pool in Figure 1a), which is believed to result from nonuniformity in the gradient. Residual errors of this type can, if necessary, be calibrated out by reference to such profiles; they were ignored in the results presented here, because the correction cancels out in the final calculation of hydrocarbon saturation (Eq. 5). Sensitivity at the bottom (corresponding to the calibration volume in Figure 1a) was essentially flat.

In addition to these hardware factors, the overall result in our hydrodynamic experiment is subject to random and sys-

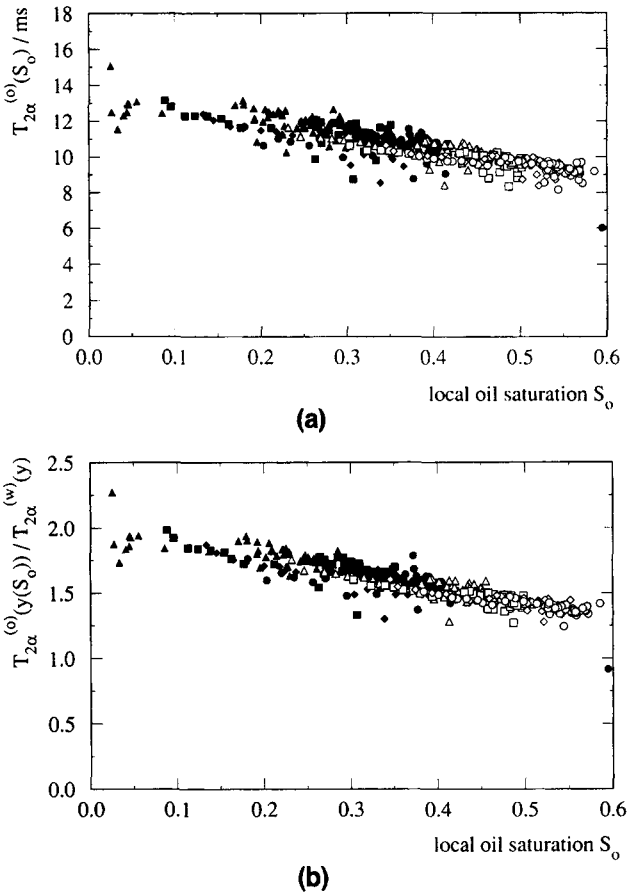

Figure 10. (a) Scatter plot of the hydrocarbon $T_{2\alpha}^{(o)}$ values against the corresponding local hydrocarbon saturation (data of Figure 8); (b) data of (a), but $T_{2\alpha}^{(o)}$ data plotted as a ratio of the local $T_{2\alpha}^{(w)}$ values found for the water saturated reference state in Figure 5b.

Points from pixels not clearly within the rock (inlet distributor, trapped dodecane drop) have been eliminated. Volumetric flows identified by the same symbols as in Figure 8.

tematic errors arising from the modeling assumptions involved in the relaxation data fitting. Without an improved theoretical understanding of transverse relaxation for fluids in porous media, further assessment of accuracy is difficult. We, however, have compared the integrated result in our *final* saturation profile to the mean hydrocarbon saturation obtained gravimetrically from buoyancy data (Table 4, first row).

Further corrections may be made to both NMR data and the gravimetric comparison. Because of the broad-line nature of fluids in porous media (Table 5) and the nonzero duration (finite bandwidth) of the 90° pulse (Figure 2), there is a small ($\approx 2\%$) loss of magnetization successfully nutated by the pulse (Roberts, 1992, and private communication). The loss is much less for the bulk liquid in the calibration volume so a small correction factor may therefore be applicable in Eq. 5. Also, the gravimetric comparison is sensitive to small air bubbles which may be trapped in the cell and migrate into the core. We detected a small bubble in the calibration volume by full imaging at the start of the experiment, which rapidly disappeared on flowing hydrocarbon. A correction to the gravimetric data was made using an estimate of the bubble size from the NMR image. The results (Table 4, second row) then agree within the assessed errors of the gravimetric method.

Table 4. Comparison of Mean Oil Saturation Estimates for the Final State from NMR Imaging and an Independent Gravimetric Determination*

NMR Imaging	Gravimetric		
S_o (profile average)	S_o (errors)	S_{air} (errors)	Discrepancy
0.498 (average of 63- and 64-pixel sums)	0.525 ± 0.008	0.007 ± 0.006	−0.027
0.508 (corrected for linewidth effect: see text)	0.509 ± 0.008 (estimated air bubble correction)	0.013	−0.001

*Calculated NMR results presented to 3 figures for comparison, but accuracy at this level should not be inferred. First row, NMR data from Figure 8a compared with gravimetric data; second row, same data, but with NMR data corrected for the nonzero linewidth effect (see text), and gravimetric data corrected for small changes in S_{air} arising from a small air bubble seen in initial images of the calibration volume (see text).

Given the nature of the experiment and the modeling assumptions made in data analysis, such close agreement is, no doubt, fortuitous; a comprehensive error budget for the NMR experiment is still warranted with comprehensive checks against independent determinations. Nevertheless, Table 4 illustrates the quantitative potential of the method, given adequate attention to detail. Similar conclusions have been reached by others (Chen et al., 1992b).

Conclusions

A steady-state experiment for relative permeability determinations in which phase saturation gradients are expected to exist has been used with a natural limestone sample in conjunction with ^{1}H NMR imaging. With isotopic substitution in the aqueous phase, phase discrimination is unambiguous. A profile method is sufficient to accommodate the essentially one-dimensional character of the fluid flow experiment, and the short data acquisition time allows detailed examination of transverse relaxation. Standard two-dimensional images supplement detailed interpretation of the profiles, even when full quantification is not attempted.

Bulk T_1 relaxation data showed the material to be water-wet and yielded an indication of pore-size distribution in broad agreement with mercury porosimetry. In drainage, the dodecane saturation profiles validate the assumptions of the steady-state method of Ramakrishnan and Cappiello (1991). The permanency of the capillary end-effect, with vanishing exit oil

Table 5. Lineshapes and Widths for the Specimen in Two States

Specimen State	Approx. Lineshape	$\Delta\nu_l$/Hz (FWHM)	T_2^*/ms
Water saturated	Lorentzian	276	1.15
Mixed-phase saturation (D_2O/dodecane)	Lorentzian	272	1.17

*Linewidth from a uniform phantom of the same size as the rock specimens was usually of the order of 40 Hz.

saturation, is clearly demonstrated, and the profile shapes broadly agree with qualitative predictions that they be monotonic, nonintersecting, and convex. Although not worked out in this article, quantitative verification of the fluid flow theory may now be addressed from the measured profiles.

Making use of the phase saturation gradients in the experiment, $T_{2\alpha}^{(o)}$ is seen to be a decreasing function of local hydrocarbon saturation S_o; assumptions that it may be treated as a constant and the system calibrated against a standard of the same T_2 cannot in general be correct.

For accurate results, attention to detail in the hardware preparation and calibration is required. While a single datum cannot be considered indicative of routinely achievable accuracy, we do nevertheless obtain agreement within 3% of pore volume between an independent gravimetric determination of the final state mean saturation and the corresponding integrated NMR profile.

The detailed error budget still warranted for the NMR method has not been attempted, but the principal contributions to it are identified. Especially important are the associated phenomena of inhomogeneous broadening, and diffusion-dominated transverse relaxation. These cause losses of transverse magnetization which are both significant and difficult to quantify. In the absence of any comprehensive theory of transverse relaxation for fluids in porous media, some empirical modeling assumptions are necessary. An improved theoretical understanding of transverse relaxation in confined geometries, as recently addressed by Mitra and Le Doussal (1991) and Le Doussal and Sen (1992), is clearly desirable.

Acknowledgment

We thank Dr. Herchel Smith for his generous endowment of the laboratory (L.D.H.). E. J. F. thanks the Royal Society and the SERC (United Kingdom) for an Industrial Fellowship and Schlumberger for leave of absence. The rock core holder was realized by the craftmanship of T. Bailey, who also advised on its mechanical design and constructed the probe support frame. J. Cook advised on pressure vessel safety. C. Bunch donated the carbon resistors and ably maintained the NMR hardware. The program *cmrfit* used for all the relaxation analyses apart from that of Figure 3 is part of the local *CaMReS* package and was written by N. J. Herrod and J. J. Attard. The numerical algorithm used to derive the results of Figure 3 was written and provided by A. Sezginer. S. J. Gibbs provided a PFGSE measurement of the dodecane diffusion coefficient. We thank also R. L. Kleinberg and T. A. Carpenter for valued discussions, and a referee for pointing out related work not known to us at the time of writing.

Notation

a = pore volume to surface ratio, m
B_0 = main magnet static field (z-direction), T
B_1 = applied r.f. field in transverse (x, y) plane, T
D = molecular diffusivity, $m^2 \cdot s^{-1}$
G_y = field gradient $\partial B_0/\partial y$, $T \cdot m^{-1}$
g_0 = background field gradient in rock pore space, $T \cdot m^{-1}$
g = general decay model (Eq. 2), dimensionless
h = spatial resolution, m
i = data set label
$\mathrm{i} = \sqrt{-1}$
k = rock hydraulic permeability, m^2
k_{ro} = relative permeability to hydrocarbon, dimensionless
k_y = spatial frequency (cyclic wavenumber) defined by $2\pi k_y = \gamma G_y t$, m^{-1}
L_{rock} = length of rock sample, m
$\mathcal{L}$ = lineshape or point spread function, m^{-1}
M_0 = total magnetization at zero echo time, digitizer units
M = magnetization, digitizer units
N = number of T_E values, dimensionless
p_c = capillary pressure, Pa
q = superficial flow velocity, $m \cdot s^{-1}$
Q = resonator quality factor, dimensionless
s = overall scale factor between detected signal and specimen proton content, digitizer units
S_{air} = air saturation fraction, dimensionless
S_o = hydrocarbon ("oil") saturation fraction, dimensionless
S_w = D_2O ("water") saturation fraction, dimensionless
$\mathcal{S}$ = detected time-domain signal, digitizer units
t = time from center of acquired signal, s
t_{CP} = pulse half-spacing in CPMG pulse sequence, s
t_H = time between end of 90° pulse and center of 180° pulse
T_1 = longitudinal relaxation time, s
$1/T_{1S}$ = longitudinal relaxation rate for surface relaxation processes, s^{-1}
$T_{1\alpha}$ = longitudinal relaxation time in stretched exponential model, s
T_2 = transverse relaxation time, s
$T_{2\alpha}$ = transverse relaxation time in stretched exponential model (Eq. 3), s
T_2^* = exponential timescale of free induction decay, s
$1/T_2^\bullet$ = $1/T_2^* - 1/T_2$, s^{-1}
T_{Aq} = data acquisition time for a single echo, s
T_D = additional delays in Figure 2, s
T_E = echo time (time between end of 90° pulse and center of data acquisition window), s
T_R = repolarization delay allowed between scans, s
$\bar{v}$ = mean interstitial (pore space) flow velocity, $m \cdot s^{-1}$
V_{calib} = volume of calibration volume in Figure 1a, m^3
V_{rock} = bulk volume of rock specimen, m^3
x = lateral coordinate, m
$\boldsymbol{x}$ = position vector (x, y, z)
y = vertical coordinate, m
z = horizontal coordinate (parallel to B_0), m

Superscripts

(i) = members of multiple profile sets
(o) = hydrocarbon ("oil") signal from specimen in mixed phase (D_2O and dodecane) state
(w) = water signal from specimen in fully water saturated state
$'$ = dummy variable of integration

Greek letters

α = exponent in stretched ($\alpha < 1$) or compressed ($\alpha > 1$) exponential model, Eq. 3, dimensionless
γ = gyromagnetic ratio of the proton, $rad \cdot s^{-1} \cdot T^{-1}$
$\Delta\nu_p$ = frequency interval between pixels in images, Hz
$\Delta\nu_l$ = natural linewidth (at half maximum) of fluids in specimen, Hz
μ_o = dynamic viscosity of hydrocarbon phase, Pa·s
ν = nuclear precession frequency, Hz
ν_L = nuclear resonance (Larmor) frequency, Hz
ρ_1 = longitudinal surface relaxivity, $m \cdot s^{-1}$
ϱ = local number density of ^1H nuclei, m^{-3}
$\bar{\varrho}_s$ = section average (Eq. 1) density of ^1H nuclei, m^{-1}
ϕ = local porosity (section average) of specimen, dimensionless
$\bar{\phi}$ = average porosity of specimen, dimensionless
χ^2 = mean square misfit of model to data (defined in text), dimensionless

Literature Cited

Abragam, A., *Principles of Nuclear Magnetism*, Clarendon Press, Oxford (1961).

Banavar, J. R., and L. M. Schwartz, "Probing Porous Media with Nuclear Magnetic Resonance," *Molecular Dynamics in Restricted Geometries*, J. Klafter and J. M. Drake, eds., Wiley, p. 273 (1989).

Borgia, G. C., R. J. S. Brown, P. Fantazzini, J. Gore, P. Mansfield, B. Maraviglia, E. Mesini, and L. Sgubini, eds., *Proc. Int. Meeting on Recent Advances in NMR Applications to Porous Media*, Bo-

logna, Italy (Nov. 14–16, 1990); *Magn. Reson. Imaging*, **9**, 5, entire issue (1991a).
Borgia, G. C., P. Fantazzini, G. Fanti, E. Mesini, L. Terzi, and G. Valdrè, "A Proton Relaxation Study of Immiscible Liquid Arrangement in Microporous Structures," *Magn. Reson. Imaging*, **9**, 695 (1991b).
Bracewell, R. N., *The Fourier Transform and Its Applications*, McGraw Hill, Tokyo, 2nd ed. (1978).
Brownstein, K. R., and C. E. Tarr, "Importance of Classical Diffusion in NMR Studies of Water in Biological Cells," *Phys. Rev. A*, **19**(6), 2446 (1979).
Buckley, J. S., K. Takamura, and N. R. Morrow, "Influence of Electrical Surface Charges on the Wetting Properties of Crude Oils," *S.P.E. Reservoir Eng.*, **4**, 332 (1989).
Butler, J. P., J. A. Reeds, and S. V. Dawson, "Estimating Solutions of First Kind Integral Equations with Non-negative Constraints and Optimal Smoothing," *SIAM J. Numer. Anal.*, **18**(3), 381 (1981).
Callaghan, P. T., *Principles of Nuclear Magnetic Resonance Microscopy*, Clarendon Press, Oxford (1991).
Carr, H. Y., and E. M. Purcell, "Effects of Diffusion on Free Precession in Nuclear Magnetic Resonance Experiments," *Phys. Rev.*, **94**(3), 630 (1954).
Chen, S., K.-H. Kim, F. Qin, and A. T. Watson, "Quantitative NMR Imaging of Multiphase Flows in Porous Media," *Magn. Reson. Imaging*, **10**, 815 (1992a).
Chen, S., F. Qin, K.-H. Kim, and A. T. Watson, "NMR Imaging of Multi-phase Flows in Porous Media," *Proc. Tech. Conf. of the S.P.E.*, Washington, DC, 1013, SPE preprint no. 24760 (1992b).
Collins, R., *Flow of Fluids through Porous Materials*, Reinhold, New York (1961).
de Crespigny, A. J., "Spatial Localisation in Nuclear Magnetic Resonance Imaging and Spectroscopy," PhD Diss., Univ. of Cambridge, School of Clinical Medicine, Chap. 3 (1991).
Daniell, G. J., "Of Maps and Monkeys," *Maximum Entropy in Action*, 1, B. Buck and V. A. Macaulay, eds., Clarendon Press, Oxford (1991).
Davies, S., and K. J. Packer, "Pore Size Distributions from Nuclear Magnetic Resonance Spin-Lattice Relaxation Measurements of Fluid-Saturated Porous Solids: I. Theory and Simulation," *J. Appl. Phys.*, **67**(6), 3163 (1990).
Dereppe, J.-M., C. Moreaux, and K. Schenker, "Two-Dimensional Spin-Echo and Three-Dimensional Chemical Shift Imaging Techniques for Analysis of Oil-Water Replacement in Limestone," *J. Magn. Reson.*, **91**, 596 (1990).
Le Doussal, P., and P. N. Sen, "Decay of Nuclear Magnetisation by Diffusion in a Parabolic Magnetic Field: an Exactly Solvable Model," *Phys. Rev. B*, **46**(6), 3465 (1992).
Edelstein, W. A., J. M. S. Hutchison, G. Johnson, and T. Redpath, "Spin-Warp NMR Imaging and Application to Human Whole-Body Imaging," *Phys. Med. Biol.*, **25**(4), 751 (1980).
Fordham, E. J., T. P. L. Roberts, T. A. Carpenter, L. D. Hall, and C. Hall, "Dynamic NMR Imaging of Rapid Depth Filtration of Clay in Porous Media," *AIChE J.*, **37**(12), 1900 (1991).
Gallegos, D. P., and D. M. Smith, "An NMR Technique for the Analysis of Pore Structure: Determination of Continuous Pore Size Distributions," *J. Coll. Int. Sci.*, **122**(1), 143 (1988).
Graue, A., K. Kolltveit, J. R. Lien, and A. Skauge, "Imaging Fluid Saturation Development in Long Core Flood Displacements," *S.P.E. Formation Evaluation*, **5**(4), 406 (1990).
Gummerson, R. J., C. Hall, W. D. Hoff, R. Hawkes, G. N. Holland, and W. S. Moore, "Unsaturated Water Flow within Porous Materials Observed by NMR Imaging," *Nature*, **281**, 56 (1979).
Hahn, E. L., "Spin Echoes," *Phys. Rev.*, **80**(4), 580 (1950).
Hall, L. D., T. Marcus, C. Neale, B. Powell, J. Sallos, and S. L. Talagala, "A Modified Split-Ring Resonator Probe for NMR Imaging at High Field Strengths," *J. Magn. Reson.*, **62**, 525 (1985).
Hall, L. D., V. Rajanayagam, and C. Hall, "Chemical-Shift Imaging of Water and *n*-Dodecane in Sedimentary Rocks," *J. Magn. Reson.*, **68**, 185 (1986).
Honeyborne, D. B., *The Building Limestones of France*, H.M.S.O., London (1982).
Horsfield, M. A., L. D. Hall, and C. Hall, "Two-Species Chemical Shift Imaging Using Prior Knowledge and Estimation Theory: Application to Rock Cores," *J. Magn. Reson.*, **87**, 319 (1990).
Kenyon, W. E., P. I. Day, C. Straley, and J. F. Willemsen, "A Three-Part Study of NMR Longitudinal Relaxation Properties of Water Saturated Sandstones," *S.P.E. Formation Evaluation*, 622 (Sept., 1988).
Kenyon, W. E., J. J. Howard, A. Sezginer, C. Straley, and A. Matteson, "Pore Size Distributions and NMR in Microporous Cherty Sandstones," *S.P.W.L.A. Logging Symp.*, 1 (June 11–14, 1989).
Kleinberg, R. L., and M. A. Horsfield, "Transverse Relaxation Processes in Porous Sedimentary Rock," *J. Magn. Reson.*, **88**, 9 (1990).
Latour, L. L., R. L. Kleinberg, and A. Sezginer, "Nuclear Magnetic Resonance Properties of Rocks at Elevated Temperatures," *J. Coll. Int. Sci.*, **150**, 535 (1992).
Majors, P. D., J. L. Smith, F. S. Kovarik, and E. Fukushima, "NMR Spectroscopic Imaging of Oil Displacement in Dolomite," *J. Magn. Reson.*, **89**, 470 (1990).
Mandava, S. S., A. T. Watson, and C. M. Edwards, "NMR Imaging of Saturation during Immiscible Displacements," *AIChE J.*, **36**(11), 1680 (1990).
Mansfield, P., and P. G. Morris, "NMR Imaging in Biomedicine," *Adv. Mag. Res., Suppl. 2*, Academic Press (1982).
Marle, C. M., *Multi-Phase Flow in Porous Media*, Éditions Technip, Paris (1981).
Meiboom, S., and D. Gill, "Modified Spin-Echo Method for Measuring Nuclear Relaxation Times," *Rev. Sci. Instrum.*, **29**(8), 688 (1958).
Mitra, P. P., and P. Le Doussal, "Long-Time Magnetisation of Spins Diffusing in a Random Field," *Phys. Rev. B*, **44**(21), 12035 (1991).
Morris, P. G., *NMR Imaging in Medicine and Biology*, Clarendon Press, Oxford (1986).
Murphy-Boesch, J., G. J. So, and T. L. James, "Precision Mapping of the B_1 Field Using the Rotating Frame Experiment," *J. Magn. Reson.*, **73**, 293 (1987).
Osment, P. A., K. J. Packer, M. J. Taylor, J. J. Attard, T. A. Carpenter, L. D. Hall, N. J. Herrod, and S. J. Doran, "NMR Imaging of Fluids in Porous Solids," *Phil. Trans. A Roy. Soc. Lond.*, **333**, 441 (1990).
Parsons, R. W., "Microwave Attenuation—a New Tool for Monitoring Saturations in Laboratory Flooding Experiments," *S.P.E. J.*, 302 (Aug. 1975).
Ramakrishnan, T. S., and A. Cappiello, "A New Technique to Measure Static and Dynamic Properties of a Partially Saturated Porous Medium," *Chem. Eng. Sci.*, **46**(4), 1157 (1991).
Ramakrishnan, T. S., and D. T. Wasan, "Two-Phase Distribution in Porous Media: an Application of Percolation Theory," *Int. J. Multiphase Flow*, **12**, 357 (1986).
Roberts, T. P. L., "Design of Radio-Frequency Pulses for Use in Nuclear Magnetic Resonance Imaging and Localised Spectroscopy," PhD Diss., School of Clinical Medicine, Univ. of Cambridge, U.K. (Feb., 1992).
Rothwell, W. P., and H. J. Vinegar, "Petrophysical Applications of NMR Imaging," *Appl. Optics*, **24**(23), 3969 (1985).
Slichter, C. P., *Principles of Magnetic Resonance*, Springer-Verlag, Berlin (1990).
Vinegar, H. J., "X-Ray C.T. and NMR Imaging of Rocks," *J. Petrol. Technol.*, 257 (Mar., 1986).

Appendix: Outline of NMR Imaging Theory

We outline the connection between the primary experimental data (digitized signals) and the image profiles reported. The pulse sequence used is illustrated in Figure 2. The gradient G_y encodes spatial location y as a frequency offset $\nu - \nu_L = (\gamma/2\pi)G_y y$ from the precession frequency $\nu_L = (\gamma/2\pi)B_0$ of the detected nucleus, where γ is the gyromagnetic ratio of the nucleus. The signal $S(t)$ in the heterodyne detection frame (referenced to ν_L) is then the superposition of all the spin-echo signals arising from different regions of the sample with different local proton densities $\varrho(x)$. For the sake of clarity of exposition only, we model (*in this Appendix alone*) the transverse relaxation behavior by a simple exponential function and the intrinsic echo shape by a double-sided exponential of timescale T^*_2. [This timescale differs only slightly from the usual

timescale T_2^* of an exponential free induction decay ($1/T_2^* = 1/T^*_2 + 1/T_2$), because usually $T_2^* \ll T_2$.] Then, within a scale factor s:

$$\frac{1}{s}\,\mathcal{S}(t;T_E) = \int_{\text{volume}} \varrho(x)\exp[-(T_E+t)/T_2(x)] \times \exp(-|t|/T_2^*)\exp(i\gamma G_y y t)\,dx \quad \text{(A1)}$$

where $t=0$ is taken to be at the center of the main spin echo. Note that as a Fourier integral of a real function, the (complex) signal is expected to be Hermitian. Departures from the model forms assumed for the relaxation are discussed in the main text.

The usual image transform (making the conventional substitution $2\pi k_y = \gamma G_y t$) is:

$$M(y;T_E) = \int_{-\infty}^{\infty} \mathcal{S}(k_y;T_E)\exp(-2\pi i k_y y)\,dk_y \quad \text{(A2)}$$

which is related to the actual proton density distribution $\varrho(x)$ by:

$$\frac{1}{s}\,M(y;T_E) = \int_{\text{specimen}} \bar{\varrho}_s(y') \times \exp[-T_E/T_2(y')]\,\mathcal{L}(y-y')\,dy' \quad \text{(A3)}$$

where $\bar{\varrho}_s(y)$ is the section-average proton density defined in Eq. 1, $\mathcal{L}(y)$ is the Fourier transform of the echo shape:

$$\mathcal{L}(y) = \int_{\infty}^{\infty} \exp(-2\pi|k_y|/\gamma G_y T_2^*)\exp(-2\pi i k_y y)\,dk_y \quad \text{(A4)}$$

and we have assumed that $T_2(x)$ is uniform over (x, z) sections. We also neglect in Eq. A4 a time-dependent factor $\exp[-t/T_2(x)]$, because typically $T_2 \gg T^*_2$. We thus see Eq. A3 that the usual image transform (Eq. A2) yields a magnetization profile $M(y; T_E)$, which within the scale factor s is the section-average proton density $\bar{\varrho}_s(y)$ (Eq. 1), subject to (i) blurring by convolution with a point spread function $\mathcal{L}(y)$ and (ii) decay by transverse relaxation $\exp[-T_E/T_2(y)]$.

The lineshape blurring imposes a limit on spatial resolution which is of order $2\pi\Delta\nu_l/\gamma G_y$ where $\Delta\nu_l$ is the linewidth in Hz ($\Delta\nu_l = 1/\pi T^*_2$ for the Lorentzian model adopted here). This can be important with porous media, but in this work the resolution limit imposed by the digitization was in fact coarser. In practice, the digital Fourier transform approximation to Eq. A2 is calculated from records of finite length T_{Aq}; for the DFT (Bracewell, 1978), the pixel width (in Hz) $\Delta\nu_p = 1/T_{Aq}$ showing that fine pixel resolution (small $\Delta\nu_p$) requires a long T_{Aq}, possibly inconsistent with a requirement for a short $T_E = T_{Aq} + 2T_D$ (Figure 2). Spatial resolution h at a given G_y may thus be limited either by linewidth or by a requirement for a short echo time T_E:

$$h = \frac{2\pi}{\gamma G_y}\max[f_l\Delta\nu_l, f_p\Delta\nu_p] \quad \text{(A5)}$$

The prefactors f_l and f_p indicate some latitude in the criterion of "resolution."

In the present work, a sine-bell data window was imposed on the digitized data to suppress truncation artifacts ("ringing" at sharp edges) in the digital version of Eq. A2. This window imposes its own point spread function which is approximately 1.6 pixels wide at half-height and 3 pixels wide between its first zeros. This suggests that $f_p = 2$ (say) should be taken in Eq. A5. For a Lorentzian line, significant signal occurs in the "wings" of the lineshape; taking the width at 10% height as the criterion for "just-resolved" requires $f_l = 3$ in Eq. A5. For our material (Table 5) and experimental choices (Figure 2), the two terms in Eq. A5 are then 0.8 mm and 1.6 mm, respectively. Sampling and windowing are thus the limiting factors on resolution here; the continuous convolution with $\mathcal{L}(y)$ in Eq. A3 may be replaced with a discrete convolution with the data windowing point spread function. This results in blurring by approximately 2 pixels in 128. Provided that variations in the image are sufficiently smooth over such scales, the consequent bias will be small and is henceforth neglected also. Subject to these approximations, we then have:

$$\frac{1}{s}\,M(y;T_E^{(i)}) = \bar{\varrho}_s(y)\exp[-T_E/T_2(y)]. \quad \text{(A6)}$$

There is scope for more sophisticated data processing methods on the relatively coarsely sampled data (128 pixels) which we acquired (Daniell, 1991), but in this work we have followed the orthodox procedures.

Manuscript received Oct. 19, 1992, and revision received Feb. 16, 1993.